The critical role of composition-dependent planar defects in the performance of $MA_{1-x}FA_xPbI_3$ perovskite solar cells

Wei Li[1,2,12], Mathias Uller Rothmann [3,12], Ye Zhu[4,12], Weijian Chen[5], Chenquan Yang[1], Yongbo Yuan[6], Yen Yee Choo[3], Xiaoming Wen[5], Udo Bach[7,8,9,10*], Yi-Bing Cheng[2,1,*], Joanne Etheridge[3,11,*]

Affiliations:

1. State Key Laboratory of Advanced Technology for Materials Synthesis and Processing, Wuhan University of Technology, Wuhan, 430070, P. R. China.
2. Foshan Xianhu Laboratory of the Advanced Energy Science and Technology Guangdong Laboratory, Xianhu Hydrogen Valley, Foshan, 528200, P. R. China
3. Department of Materials Science and Engineering, Monash University, Victoria 3800, Australia.
4. Department of Applied Physics, Research Institute for Smart Energy, The Hong Kong Polytechnic University, Hung Hom, Kowloon, Hong Kong.
5. Centre for Micro-Photonics, Swinburne University of Technology.
6. Hunan Key Laboratory of Super Microstructure and Ultrafast Process, School of Physics and Electronics, Central South University, Changsha, Hunan, 410083, P. R. China
7. Department of Chemical Engineering, Monash University, Victoria 3800, Australia.
8. ARC Centre of Excellence in Exciton Science, Monash University, Victoria 3800, Australia.

9. Commonwealth Scientific and Industrial Research Organization, Manufacturing Flagship, Clayton, Victoria 3168, Australia.

10. Melbourne Centre for Nano fabrication, 151 Wellington Road, Clayton, VIC 3168, Australia.

11. Monash Centre for Electron Microscopy, Monash University, Victoria 3800, Australia.

12. Wei Li, Mathias Uller Rothmann and Ye Zhu contributed equally to this work.

* Corresponding author. Email: joanne.etheridge@monash.edu (J.E.); yibing.cheng@whut.edu.cn (Y.B.C.); udo.bach@monash.edu (U.B.)

Abstract

Perovskite solar cells (PSCs) show excellent power conversion efficiencies, long carrier diffusion lengths and low recombination rates. This encourages a view that intragrain defects are electronically benign with little impact on device performance. Here we vary methylammonium (MA)/ formamidinium (FA) composition in $MA_{1-x}FA_xPbI_3$ (x=0-1), and compare the structure and density of intragrain planar defects with the device performance, otherwise keeping the device nominally the same. We find charge carrier lifetime, open-circuit voltage-deficit, and current-voltage hysteresis correlate with the density and structure of $\{111\}_c$ planar defects (x=0.5-1) and $\{112\}_t$ twin boundaries (x=0-0.1). The best performance parameters are found when essentially no intragrain planar defects are evident (x=0.2). Similarly, reducing the density of $\{111\}_c$ planar defects using MASCN-vapour-treatment of $FAPbI_3$ (x~1), also improved performance. These observations suggest that intragrain defect control can provide an important route for improving PSCs' performance, in addition to well-established parameters, such as grain boundaries and heterojunction interfaces.

Main Text

Organic-inorganic hybrid perovskites have become exciting candidates for use in next generation solar cells due to their astonishing power conversion efficiencies (PCE) combined with a relatively simple and low-cost processing route. Given that they can be processed at relatively low temperatures, with rapid nucleation and crystallisation from solution, a non-negligible level of structural defects is expected, including intragrain planar defects and point defects.[1,2] Intragrain defects, such as stacking faults (SFs), twins, and dislocations, in more established photovoltaic materials, such as silicon[3] and CdTe,[4] have been identified as a major cause of recombination, limiting the PCE. Enormous efforts have been made to minimize the defect density and the associated recombination rate.[4] In contrast, relatively little is known about nature of the intragrain defects in hybrid halide perovskite solar cells (PSC).

The reasons are two-fold: Firstly, the structure of hybrid perovskites can be easily damaged by probes such as electron beams or mechanical tips,[5-7] making it challenging to obtain reliable local structural information; Secondly, the extraordinary performance of hybrid perovskites, especially their long charge carrier diffusion lengths and low recombination rates,[8] has led to a widely-accepted belief that any intragrain defects must be electronically benign and have a relatively minor effect on the non-radiative recombination and open-circuit voltage (V_{OC}) of devices, (compared with grain boundaries and interlayer defects).[1,9-11] This is supported by first-principle calculations which suggest that the type of defects in $MAPbI_3$ that would contribute deep levels in the bandgap have high formation energies, and that the dominant defects only generate shallow-level states near band edges.[9]

In this context, efforts to improve device performance have focussed on passivating the defect states at the heterojunction interface and grain boundaries.[11] Whereas, the presence and structure of intragrain defects, and hence their impact on PSC performance, have not yet been adequately investigated. This is underscored by recent theoretical [12] and experimental [13] studies that have suggested that $\{111\}_c$ twin domains in $Cs_{0.125}FA_{0.875}PbI_2Br$, and $Cs_{0.05}FA_{0.81}MA_{0.14}PbI_{2.55}Br_{0.45}$, respectively, may affect device performance [12,13] and that $\{110\}_c$ twin domains in $MAPbI_3$ may contribute to J-V hysteresis through ferroelectric poling,[14] questioning the benign role of some intragrain defects. (Throughout this manuscript, the subscripts "t"' and "c" denote indexing in the tetragonal and cubic phase, respectively, and 'performance' refers collectively to PCE, V_{oc} and J-V hysteresis.)

In this work, we investigate the impact of intragrain defects in hybrid halide $MA_{1-x}FA_xPbI_3$ on the PSC performance. This is achieved through a combination of: defect engineering in $MA_{1-x}FA_xPbI_3$ via varying MA/FA composition, while otherwise keeping the device materials and configuration nominally the same; ultralow-dose transmission electron microscopy (TEM) to characterise *reliably* the nature of these defects; and correlation of the measured intragrain defect structures with the measured PSC performance. We identify two types of intragrain planar defects with their density controllable by varying the MA/FA ratio and, in the case of $FAPbI_3$, through methylammonium thiocyanate (MASCN) vapour treatment. We observe an empirical correlation between their structure, density and device performance. While we cannot completely isolate the role of planar defects from other parameters, our collective results suggest that planar defect control can provide an additional avenue for device optimization, in addition to critical parameters, such as grain boundaries and heterojunction interfaces.

Defect Structure versus Composition

The Goldschmidt's *tolerance factor* (*t*) provides a simple geometric indicator of perovskite stability, with $t\sim1$ predicting a stable cubic phase. Using the tolerance factor as a rough guide, we consider the impact of varying x in $MA_{1-x}FA_xPbI_3$ on structural stability and the related propensity for defect structures in **Supplementary Discussion 1**. Changing the proportion of smaller MA to larger FA cations changes t, encouraging the formation of different planar defects for $t<1$ and $t>1$ and discouraging them when $t\sim1$. To test this experimentally, we examine $MA_{1-x}FA_xPbI_3$ using ultralow-dose TEM conditions (electron dose≤10 eÅ^{-2}),[7,15] complemented by X-ray diffraction (XRD) (**Figure 1, 2a-b**). (Note that the value, x, is nominal, derived from the compositions of the perovskite precursor solutions.)

The TEM image of **$MAPbI_3$ (x=0, t=0.957**) displays 100-300 nm wide twin domains with $\{112\}_t$ boundaries **(Figure 1a)**, as described previously.[19] The corresponding selected area electron diffraction (SAED) pattern shows twinned diffraction spots (**Figure 1b** insert). Most grains are oriented close to $<1\bar{1}0>_t$ (from XRD, **Figure 2a**), so that the twins are visible in TEM images of an untilted film. From this, we showed almost all grains are twinned.[19] The angular separation between the twinned reflections is directly related to the "tetragonality" defined as d_{002t}/d_{110t} (**Supplementary Table 1**).

From the TEM images, about half the **$MA_{0.9}FA_{0.1}PbI_3$ (x=0.1, t=0.965)** grains have $\{112\}_t$ twin domains (**Figure 1c**), with a similar width to the pure MA compound. (From XRD, most grains are again oriented close to $<110>_t$ (**Figure 2a**)). The separation between the twinned reflections in the corresponding SAED patterns (**Figure 1d**) is smaller, indicating a reduced tetragonality with increased FA composition (as anticipated in **Supplementary Discussion 1**). Some grains are not twinned, as indicated by the absence of twin contrast and twin reflections (**Supplementary Figure 1**), but nevertheless are found to have a tetragonality just greater than one. As the tolerance factor is close to one, the driving force for twin formation becomes marginal. It may be that grains with a locally higher FA composition and/or smaller grain size may not form twins.

In $MA_{0.8}FA_{0.2}PbI_3$ (x=0.2, t=0.972) no striped contrast or twinned reflections are observed from a study of more than 1000 grains (**Figures 1e, 1f and Supplementary Figure 21**), and the lattice parameters are metrically cubic (a=b=c), tetragonality=1, removing the driver for $\{112\}_t$ twinning. (Note that, although the structure is metrically cubic, at a local level the structure cannot have a cubic space group.) $t = 0.972$ may be taken as a reference tolerance factor above which a tetragonal structure is prohibited in $MA_{1-x}FA_xPbI_3$. Indeed, increasing the FA concentration further, yields a metrically cubic structure with no $\{112\}_t$ twinning (**Figures 1g-l**).

For both x=0.1 and 0.2, we note the absence of superlattice reflections, suggesting that MA and FA exist in solid solution and do not order on the A-site, consistent with previous x-ray analysis.[16] For x=0, 0.1 and 0.2, there is no detectable variation in lattice parameters within a grain, within the measurement precision of ±0.004 Å (see **Supplementary Discussion 2**).

Once the FA content reaches 50% or more **(x≥0.5, t~1 to 1.036)**, we observe a fundamental change in defect structure - a different type of twinning or SF, with $\{111\}_c$ boundaries, within a metrically cubic lattice. We first describe this structure, and its relationship to a hexagonal phase, before detailing the experimental evidence.

A typical form of hexagonal intergrowth in a cubic lattice is via $\{111\}_c$ twin boundaries, where the local stacking changes from ABCABC (cubic $\{111\}_c$ stacking) to ABAB (2H hexagonal (0001) stacking). Similarly, a 2H hexagonal $MA_{1-x}FA_xPbI_3$ **(Figure 3a, 3b)** phase can coexist with the cubic phase at twin boundaries or SFs, with a $\{111\}_c$ twin boundary shown in **Figure 3c** (the A-B-A lamella) and a $\{111\}_c$ SF shown in **Figure 3h** (the A-B-A-B lamella). As *t* increases beyond 1, so does the driving force to form the hexagonal phase (as described in **Supplementary Discussion 1**).

In SAED patterns near the $<1\bar{1}0>_c$ (**Figures 1h-1l**) and $<001>_c$ (**Supplementary Figures 2**) zone axes of $MA_{1-x}FA_xPbI_3$ (x=0.5, 0.85 and 1) taken from individual grains, we observe, *to different extents for different compositions*, extra reflections at the $^1/_3\,111_c$ positions consistent with $\{111\}_c$ twinning, plus diffraction "streaks" parallel to $<111>_c$ generated by $\{111\}_c$ SFs, **Figures 1c-1g** (and **Supplementary Figure 3**). These correspond to the often irregular, striped contrast in the corresponding images.

Importantly, the density of $\{111\}_c$ SFs increases with FA content. For x=0.5, not all grains contain $\{111\}_c$ planar defects and those that do mostly comprise well-spaced $\{111\}_c$ twin boundaries (**Figure 1g**), giving rise to the well-resolved $^1/_3\,111_c$ reflections (**Figure 1h**). For x=0.85 and 1, all grains contain a very high density of $\{111\}_c$ SFs with the highest density in pure $FAPbI_3$. Correspondingly, the $^1/_3\,111_c$ reflections become weaker due to the smaller twin domain size (see **Figures 1h, j and l**) and are often "submerged" by diffraction streaks from $\{111\}_c$ SFs. The correspondence between the $\{111\}_c$ twins/SFs and the hexagonal phase is consistent with XRD (**Figure 2b**), where the diffraction peaks nominally associated with the hexagonal phase become stronger with increasing x (for $x \geq 0.5$).

These observations are consistent with neutron and x-ray studies indicating an increase in the hexagonal phase and $\{111\}_c$ twin boundaries with increasing x [17,18],[19,20](also predicted by density functional methods[12]). $\{111\}_c$ planar defects have also been reported in $Cs_{0.05}FA_{0.81}MA_{0.14}PbI_{2.55}Br_{0.45}$.[13]

Unlike the $\{112\}_t$ twin domains, the $\{111\}_c$ planar defects in $FAPbI_3$ persist when heated to at least 100°C (**Supplementary Figure 4**). This is consistent with the relative rigidity and low formation energy of the face-sharing octahedra at the $\{111\}_c$ boundary,[12] compared with the flexible corner-sharing octahedra of the $\{112\}_t$ boundary.

We also considered different sample preparation methods. The gas-assisted method, **Figure 1**, and the anti-solvent method, **Supplementary Figure 5,** both show similar $\{111\}_c$

planar defects, suggesting a low formation energy in $MA_{1-x}FA_xPbI_3$ ($x \geq 0.5$). However, recent structural observations of thin (30nm) films of co-evaporated $FAPbI_3$ exhibit a much lower density of SFs, suggesting the preparation route *can* influence the formation of SFs.[21] Furthermore, it has recently been shown that a MASCN-vapour treatment can convert the photo-inactive 'yellow' δ-$FAPbI_3$ phase to the photo-active 'black' α-$FAPbI_3$ phase.[22] Noting that the $\{111\}_c$ SF is a lamella of the δ-$FAPbI_3$ phase (Fig 3), we found that a MASCN-vapour treatment can control the $\{111\}_c$ SF density in the cubic α-$FAPbI_3$ phase, as discussed later (and in **Supplementary Figure 6**).

Performance versus MA/FA Composition

We measured the device performance versus composition, x, in $MA_{1-x}FA_xPbI_3$, while keeping electron/hole transport layers and device configuration nominally the same.

As the FA content increases from 0 to 1, the photoluminescence (PL) peak position shifts from 770.7 nm (1.61 eV) to 809.3 nm (1.53 eV) which results in a band gap change of just 0.08 eV (**Figure 2c and Supplementary Figure 7**). The PL intensity exhibits a super-linear increase with increasing excitation fluence in double-logarithmic coordinates (**Supplementary Figure 8**). $FAPbI_3$ shows a much larger slope (1.815) in the super-linear PL than that of $MA_{0.2}FA_{0.8}PbI_3$ (1.570) and $MAPbI_3$ (1.575), indicating a higher density of defect-trapping states in $FAPbI_3$ (See **Supplementary Discussion 3).**

The effective lifetime derived from time-resolved PL measurements (**Figure 2d**) and with varied excitation laser fluence (**Supplementary Figure 9**) have a clear maximum at x=0.2 and minimum at x=1 (**Figure 2e**). The effective lifetime of $MA_{0.8}FA_{0.2}PbI_3$ is 357 ns which is about 1.5 times longer than for x=0, 0.1 and 0.5 and 10^2 times longer than for x=0.85 and x=1. This is consistent with observations in polycrystalline thin films [23] and single crystals [24,25] of $MA_{1-x}FA_xPbI_3$.

The difference between bandgap potential (E_g/q) and open-circuit voltage (V_{OC}) of PSCs (V_{OC} deficit) (**Figure 2e**) is also a useful quick gauge of non-radiative recombination rates of the absorber.[26] In line with the lifetime results, the V_{OC} deficit is lowest for composition x=0.2 and highest for x=0.85 and 1, with x=0, 0.1 and 0.5 in between, especially for the forward scanned measurements.

PSC performance versus composition is summarised in **Figure 2f**. Photocurrent density–voltage (J-V) curves of the devices with the highest reverse scan PCE were measured (**Supplementary Figure 10)**. The diode ideality factor can be extracted from the slope of the light-dependent open-circuit voltage (V_{OC}) **(Supplementary Figure 11).**[27] As FA is added to $MAPbI_3$, $MA_{0.8}FA_{0.2}PbI_3$ shows the highest PCE from both reverse and forward scans and the lowest diode ideality factor while $FAPbI_3$ shows the poorest performance. Other studies have also found mixed MA-FA compositions in the range $0.1 \leq x \leq 0.5$ can outperform the single-cation $MAPbI_3$ and $FAPbI_3$.[23,28]

PSCs often exhibit J-V hysteresis[29] in which PCEs recorded under opposite scan conditions are different, summarised by a hysteresis index (H-index, blue triangles in **Figure 2f**), Equation (2):[30]

$$\text{Hysteresis index} = \frac{\text{PCE}_{\text{reverse}} - \text{PCE}_{\text{forward}}}{\text{PCE}_{\text{reverse}}} \qquad (2)$$

$FA_{0.8}FA_{0.2}PbI_3$ (x=0.2) exhibits the lowest hysteresis while FA-rich compositions ($x \geq 0.5$) significantly enhance hysteresis (**Figure 2f**).

To investigate the influence of ion migration on J-V hysteresis in $MA_{1-x}FA_xPbI_3$, we measured the ion migration activation energy by measuring the temperature dependent electric conductivity of $MA_{1-x}FA_xPbI_3$ films**,** following Yuan et al.[31] (**Figure 4 and Supplementary Discussion 4)**. We observed the ion migration activation energy (E_a^{ion}) increases in the order $FAPbI_3$ (0.278 eV) < $MA_{0.15}FA_{0.85}PbI_3$ (0.308 eV) < $MA_{0.8}FA_{0.2}PbI_3$ (0.409 eV) ~ $MAPbI_3$ (0.403 eV). These are comparable to previous measurements,[31,32] but in most cases are less than predicted in *single crystals* by first-principles calculations for MA^+/FA^+ and I^- ion species, particularly for high FA compositions.[32,33] The dependence of ion migration energies versus composition aligns with the observed J-V hysteresis versus composition (**Figure 2f**).

To probe spatially where the ion migration takes place, we measured I-V curves from the apparent interiors of individual grains for the compounds with the lowest ($MA_{0.8}FA_{0.2}PbI_3$) and highest ($FAPbI_3$) J-V hysteresis using conductive-atomic force microscopy (**Supplementary Discussion 5**). The hysteresis of the resulting I-V curves suggests that the apparent grain interior in $FAPbI_3$ contains ion migration channels while $MA_{0.8}FA_{0.2}PbI_3$ does not (**Supplementary Figure 12)**.

Structure versus Performance

It is striking that the best performing composition (with the longest charge carrier lifetime, lowest open-circuit-voltage deficit, current-voltage hysteresis and highest PCE) corresponds to the compound with essentially no intragrain planar defects, namely $MA_{0.8}FA_{0.2}PbI_3$. In contrast, all other compounds that have twin boundaries or SFs show significantly poorer charge carrier lifetime, open-circuit voltage deficit and current-voltage hysteresis.

Is this correlation between the presence of intragrain planar defects and performance a coincidence or causative? To address this question, we first considered each of the other factors that will change with composition and are well-known to impact performance (symmetry, band structure, grain boundaries, point defects, interfaces) (see **Supplementary Discussion 6**).[1,2,11] We find that the way these factors change with MA/FA composition does not correlate with the way the performance changes with composition. This is not to say that they do not impact performance, but their impact cannot fully account for the observed *relationship* between performance *and* composition.

In addition to the factors considered above, changing MA/FA composition may also modify other factors which we cannot easily observe. We therefore also tried to keep the bulk composition and band gap nominally the same while varying the $\{111\}_c$ SF density in $FAPbI_3$, using MASCN-vapour treatment. We observed empirically that the PCE and hysteresis improved as the SF density decreased, again in a manner that could not be solely accounted for by other factors, such as grain boundary density or surface modification (see detailed **Supplementary Discussion 7)**.

Given the above, let us consider whether and how planar defects might play a role by exploring the relationship between planar defects, composition and performance, summarized in **Figure 2e and 2f**.

The charge-carrier lifetimes of the compounds with the lower planar defect surface density (x=0, 0.1 and 0.5) are *an order of magnitude better* than the compounds with much higher planar defect surface density (x=0.85 and 1), despite the difference in the structure of the planar defects in the low density set: $\{112\}_t$ for x=0, 0.1 versus $\{111\}_c$ for x=0.5 (**Figure 2e**). (The grain and planar defect surface area densities (**Supplementary Table 2)** are plotted against properties in **Supplementary Figure 13 and 14, respectively.)**

The J-V hysteresis in the FA-rich compounds with $\{111\}_c$ planar defects (x=0.5, 0.85 and 1.0) is an order of magnitude higher than MA-rich compounds (x=0, 0.1) with $\{112\}_t$ twin boundaries, (despite a difference in planar defect surface density). Furthermore, the hysteresis increases with $\{111\}_c$ SF density.

Similarly, the activation energy for ion migration decreases significantly for FA-rich compositions (**Figure 4** and ref 32) and there are ion migration channels apparently *inside* the grains of $FAPbI_3$ (worst performance and $\{111\}_c$ SF-rich) but not *inside* the grains of $MA_{0.8}FA_{0.2}PbI_3$ (best performance and essentially planar defect free) (**Supplementary Figure 12**).

It is also important to consider whether there are plausible mechanisms by which planar defects can influence performance. We consider $\{112\}_t$ and $\{111\}_c$ defects separately, as they have fundamentally different structures (**Figure 3c**).[12]

A $\{111\}_c$ SF is equivalent to a single lamella of the photo-inactive, yellow, hexagonal δ-phase (**Figure 3h**). It is highly likely that the densely-packed $\{111\}_c$ SFs (x=0.85, 1.0) are associated with point defects. The $\{111\}_c$ SF has face-sharing octahedra, favoured by large A-site cations but leads to larger electrostatic repulsion between B-site cations due to their smaller separation.[34,35] One way to mitigate such electrostatic repulsion is to form anion vacancies in the face-sharing octahedra, reducing the valence of B-site cations and increasing the neighbouring B-B cation separations.[36,37] In the related structures, $SrMnO_3$, $BaMnO_3$ and $BaTiO_3$, it has been demonstrated that the segregation of oxygen vacancies at $\{111\}_c$ planar defects[38-41] can stabilize the nanoscale hexagonal phase.[37-44] We therefore might expect the presence of iodine vacancies at $MA_{1-x}FA_xPbI_3$ $\{111\}_c$ SFs, however, a *reliable* experimental verification is challenging as the electron beam will itself induce vacancies.[7,15]

In addition to iodine vacancies, calculations predict antisites FA_I and I_{FA} to have moderate formation energies in single crystals of pure $FAPbI_3$ [45] (**Supplementary Discussion 6.3 a**) and we speculate that these energies may be lowered at SFs.

Given a high density of iodine vacancies are expected at $\{111\}_c$ SFs, they are likely to provide ion migration channels when these SFs connect the transportation layers, both directly and via intersection with grain boundaries. These mobile ions will pile up at the heterojunction interfaces, hampering carrier extraction and leading to a more severe J–V hysteresis, as observed here, both within individual grains (**Supplementary Discussion 5, Supplementary Figure 12**) and in the device overall (**Figure 2f**).[30,46]

While isolated point defects may be relatively benign **(Supplementary Discussion 6.3)**, [9,45] the $\{111\}_c$ SFs in FA-rich $MA_{1-x}FA_xPbI_3$ (x=0.85, 1) present planar arrays with a high concentration of point defects that may provide the non-radiative recombination centres that damage performance.[45,47] Note that in the $MA_{1-x}FA_xPbI_3$ (x=0.85, 1) films, the total surface area of $\{111\}_c$ SFs is approximately 2 to 20 times larger than the total surface area of the grain boundaries (**Supplementary Table 2**), so the collective impact of SFs can be significant. In addition to harbouring point defects, $\{111\}_c$ SFs that terminate within grains (see **Supplementary Figure 15**) will induce dislocations,[41] the cores of which have dangling bonds that may act as non-radioactive recombination centres.[48]

In contrast, $MA_{0.5}FA_{0.5}PbI_3$ (with a low density of well-spaced $\{111\}_c$ twin domains, x=0.5) has a lifetime an order of magnitude better than for $MA_{1-x}FA_xPbI_3$ (x=0.85 and 1) (with high density SFs). This is consistent with DFT calculations that suggest perfect $\{111\}_c$ twin boundaries will be relatively benign electronically[12] (although note that these are zero temperature calculations and higher temperature processing may lead to defects at twin boundaries). In pure $FAPbI_3$, a 10-fold decrease in carrier lifetime in the low temperature hexagonal phase relative to the cubic phase has been partly attributed to reduced FA-cation rotational entropy imposed by the hexagonal structure.[49] Given the $\{111\}_c$ SF is a unit of the 2H hexagonal phase, the ~10^2 reduction in lifetime observed here in the SF-rich compositions (x=0.85 and 1) may be due in part to a reduction in FA rotational freedom imposed by the $\{111\}_c$ SFs.

The well-spaced, reversible and flexible corner-sharing $\{112\}_t$ twin domains in MA-rich compounds (x=0, x=0.1) are much less likely to harbour point defects and are much lower density than the $\{111\}_c$ SFs in FA-rich compounds, so they are less able to facilitate ion migration. This is consistent with the observation that the ion migration activation energies for essentially twin-free x=0.2 and twinned x=0 are comparable (**Supplementary Figure 14**), suggesting the $\{112\}_t$ twins are not acting as migration channels, unlike $\{111\}_c$ SFs. Nevertheless, it is notable that hysteresis increases with increasing density of the $\{112\}_t$

domains (albeit an order of magnitude lower than for FA-rich compounds) (**Supplementary Figure 14)**. As discussed in **Supplementary Discussion 6.2**, ion migration at grain boundaries *alone* cannot account for the observed variation in hysteresis versus composition for x=0 and x=0.1. Ferroelectricity[14] associated with the presence of $\{112\}_t$ ($\equiv\{110\}_c$) twins in pure $MAPbI_3$ has been proposed to contribute to hysteresis, *in addition* to grain boundary effects, and this would be consistent with the increase in hysteresis with the domain density with composition (**Figure 2f**).

We observe a 2-fold reduction in lifetime from the essentially twin-free cubic $MA_{0.8}FA_{0.2}PbI_3$ to $\{112\}_t$ twinned tetragonal $MA_{1-x}FA_xPbI_3$ (x=0, 0.1). This may be due to changes in twin density, phonon modes[50] and/or reduced MA/FA rotational entropy.[49]

Finally and importantly, twin boundaries and SFs in $MA_{1-x}FA_xPbI_3$ mostly terminate at the film surface and grain boundaries, introducing defects to heterojunction interfaces and grain boundaries. In this way, the change in the structure and density of twins/SFs via the MA/FA ratio can change the number and nature of the defects at GBs and interfaces. These combined effects could exacerbate the impact on device performance of any one alone.

Conclusions

We observe that tuning the FA/MA ratio in $MA_{1-x}FA_xPbI_3$, tunes the type and density of intragrain planar defects to give $\{112\}_t$ twin domains for tetragonal $0\leq x<0.2$, increasing in twin density with MA (x=0), and $\{111\}_c$ twin domains and SFs for metrically cubic $0.5\leq x\leq 1$, increasing in SF density with FA (x=1). In the 'middle' (x=0.2), $MA_{0.8}FA_{0.2}PbI_3$ is essentially planar-defect free and metrically cubic. We also observe empirically that PCE, carrier lifetime and hysteresis deteriorate with increasing density of both types of planar defects but is considerably worse for high-density $\{111\}_c$ SFs. The best performance is for essentially planar defect-free $MA_{0.8}FA_{0.2}PbI_3$ (**Figure 1 e,f**). We further observe that MASCN vapour treatment reduces $\{111\}_c$ planar defects and J-V hysteresis and improves PCE of $FAPbI_3$ PSCs, while it does not modify the crystal lattice nor band gap of the bulk α-$FAPbI_3$, (although surface modification is likely).

Our combined observations suggest that the $\{111\}_c$ stacking faults, (equivalent to a monolayer of the photo-inactive hexagonal δ-$FAPbI_3$), can harbour point defects and promote dislocations, providing ion migration channels that increase hysteresis, and act as deep recombination centres, impacting PCE. The hexagonal SF structure will also inhibit rotational entropy of the MA/FA cation, contributing to a reduction in carrier lifetime.[52] In contrast, we observe that the flexible $\{112\}_t$ twin boundaries, which harbour fewer point defects, are associated with higher ion migration energies which show little dependence on twin density, suggesting $\{112\}_t$ twins do not provide significant ion migration channels.

Planar defects also interact with grain boundaries and interfaces, and so can impact together on the PSC performance.

Device configuration, heterojunction interfaces and grain boundaries, are known to have a major impact on the performance of PSCs.[11] Here, we demonstrate that planar defects can also play a significant role, providing further scope for optimisation of this exciting PV technology via planar defect control.

Methods

Perovskite precursor solution and film preparation

Perovskite precursor solutions were prepared by dissolving stoichiometrically the desired combinations of methylammonium iodide (MAI, Dyesol), formamidinium iodide (FAI, Dyesol), and PbI_2 (Sigma) in a concentration of 1.3 M in dimethylformamide (DMF) at room temperature. An extra 0.10 g HI (57 wt% in water) was added to 1 ml of the $FAPbI_3$ and the $MA_{0.15}FA_{0.85}PbI_3$ solution. A ~300 nm thick perovskite film was then deposited by spin coating the 1.3 M (for PSC fabrication) or 0.5 M (for TEM specimen preparation) precursor solution at 6,500 rpm for 30 s, using a gas-assisted spin coating method, or anti-solvent method. For the gas-assisted method, dry N_2 gas at 40 psi was blown over on the film surface for 10 s once the spinning speed reached 6500 rpm for 3 s. For the anti-solvent method, at the time of 3 s after starting spin-coating, a 200 µL CBZ was quickly dropped as an antisolvent. The deposited precursor films were then annealed at 150 °C for 20 min (for $FAPbI_3$) or 10-20 min at 100 °C (20 min for $MA_{0.15}FA_{0.85}PbI_3$ and 10 min for all others).[51,52]

Previous XRD studies[16] have shown that the crystal structure changes from tetragonal at $x=0$ to pseudo-cubic at $x=0.2$, and cubic for $x>0.2$, remaining cubic to $x=1$. We therefore decided to investigate chemical compositions of $x= 0, 0.1, 0.2, 0.5, 0.85$ and 1. Please note that in this paper all the cation compositions of the perovskite films refer to chemical ratios in the precursor solution.

For the MASCN vapour treated $FAPbI_3$, the fabrication method is similar to the method reported by Grätzel et al.[22] A $FAPbI_3$ precursor film was deposited by spin coating the 1.3 M precursor solution at 6,500 rpm for 30 s, using a conventional anti-solvent method. From 15 s to the end, 200 µL CBZ was quickly dropped as an antisolvent. After 1 min of annealing at 100 °C, the yellow δ-phase $FAPbI_3$ film was put on top of the MASCN vapour atmosphere until the colour of the film changed from yellow to black at a temperature of 100 °C. The MASCN vapour atmosphere was generated by heating a MASCN film which was prepared by an ultrasound spray of 0.2 mg/ml (low-concentration) or 0.4 mg/ml (high-concentration) MASCN in IPA on a glass substrate. Finally, the perovskite film was further annealed at 150 °C for 20 mins.

For phenethylammonium iodide (PEAI) treatment, the PEAI solution was dissolved in isopropanol (IPA) at a concentration of 20 mM and spin-coated onto the perovskite surface at a spin rate of 5,000 rpm without any further processing.

TEM specimen preparation

Due to the organic component of hybrid perovskite, its crystal structure is easily damaged during focused gallium ion beam milling (FIB).[7] Therefore, a polycrystalline perovskite thin film was deposited directly onto a thin carbon-coated TEM grid by the method shown above in order to avoid FIB-induced damage to the perovskite structure.

TEM characterization

In order to minimize degradation due to environmental factors, the samples were placed in a sealed, nitrogen-filled container immediately after deposition and were then quickly loaded into a transmission electron microscope (a JEOL 2100F FEG-TEM with a Gatan Ultrascan camera). The total time for samples being exposed to ambient conditions was less than five minutes during loading. TEM specimens were never reused once removed from the microscope. In order to minimize possible electron beam-induced artefacts, we used a low-dose TEM imaging condition with an electron dose rate of ~2 e $Å^{-2}$ s^{-1} (unless otherwise specified). We employed a high contrast objective aperture to increase the contrast of the bright field, phase contrast images. Unless noted otherwise, all the TEM images and diffraction patterns were recorded from previously unexposed regions of the sample. In particular, the crystal grains were examined in an ‘as found’ orientation, without any attempt at crystal alignment that would have incurred further electron dose. As a result, most of our SAED patterns are not exactly aligned on a zone axis, but importantly, the essential structural information is preserved without beam-induced artefacts. To optimize the detection of structural effects, such as slight lattice parameter variations, superlattices, compositional ordering, small secondary phases, planar defects and grain boundaries, SAED patterns were taken with highly-collimated illumination to maximize angular resolution and, where appropriate, recorded with a large number of short exposures, to deliver high dynamic range.

SEM Characterisation

Except for Supplementary Figure 26, secondary electron Scanning Electron Microscopy images were taken using a FEI Magellan 400 field-emission gun SEM operating at 2kV or 5kV (as specified) using a through-lens-detector in immersion mode.

In Supplementary Figure 26, secondary electron SEM images were taken using a FEI Helios NanoLab G3 UC with field-emission gun operating at 3kV using a through-lens-detector in immersion mode.

A polycrystalline perovskite thin film was deposited directly onto a TiO_2 substrate by the method described above and placed in a sealed, nitrogen-filled container immediately after deposition for transfer and loading directly into the SEM (without coating).

Device fabrication

A dense TiO_2 blocking layer was first deposited on clean FTO glass by spray pyrolysis at 450 °C, using a bis(isopropoxide)-bis(acetylacetonate)titanium(IV) solution. After cooling to room temperature, the substrate was cut into smaller pieces of around 1 cm^2. The perovskite layer was deposited through the method listed above. Subsequently, 25 µL of spiro-OMeTAD Spiro-OMeTAD (Luminescence Technology Corp.) solution (prepared by dissolving 41.6 mg spiro-OMeTAD in 0.5 mL chlorobenzene, and adding 7.5 µL of a stock solution of 520 mg mL^{-1} lithium bis(trifluoromethylsulphonyl)imide in acetonitrile and 16.9 µL 4-tert-butylpyridine) was deposited on top of the perovskite film by spin-coating at 3000 rpm for 30 s. Finally, an 80 nm gold layer was deposited by thermal evaporation to form the complete device.

Solar cell performance characterization

Current-voltage characterization was performed using a solar simulator (Oriel) fitted with a filtered 1000 W xenon lamp to replicate AM1.5, 100 mW cm^{-2} conditions in the air. The illumination of the light source was calibrated using a silicon reference cell (Peccell Technologies) with a colour filter to minimize the spectral mismatch between the calibration diode and the PSC. The J-V response was recorded using a Keithley 2400 source meter. The PSCs were masked with a non-reflective metal aperture of 0.16 cm^{2} that defined the active area of the device. The *J-V* measurements were conducted with a 100 mV s^{-1} scan rate from forward bias to short-circuit (reverse scan) and from short-circuit to forward bias (forward scan) without any light soaking. The average PSC performances are averaged from 5 devices at each composition condition. EQE spectra were performed using a 150 W xenon lamp (Oriel) fitted with a monochromator (Cornerstone 260). EQE photocurrents were recorded under short-circuit conditions using a Keithley 2400 source meter. The monochromatic photon flux was quantified via a calibrated silicon cell (Peccell Technologies).

Other characterizations

Photoluminance

The steady state PL measurements were undertaken on a homemade system using a 405nm laser excitation source (CrystaLaser, Model BLC-050-405). The time resolved PL decay traces were measured on a Micro Time 200 (Picoquant) confocal microscopy using time correlated single photon counting (TCSPC) technique with a 470 nm laser excitation at 1 MHz repetition rate and detection through a 710 nm long pass filter. The excitation power density was around 400 mW/cm^{2}. All PL measurements were done at room temperature.

Bi-exponential fitting

The PL decay traces in **Figure** 2 (d) can be fitted to the function in equation (3):

$$I(t) = A_1 \exp\left(-\frac{t}{\tau_1}\right) + A_2 \exp\left(-\frac{t}{\tau_2}\right) \tag{3}$$

where $I(t)$ is the time dependent PL intensity, τ_1 and τ_2 are the lifetimes of the fast and the slow decay component, respectively, and A_1 and A_2 are the corresponding amplitudes. From this, we define the effective lifetime as $\tau_{\mathrm{eff}} = \frac{A_1\tau_1 + A_2\tau_2}{A_1 + A_2}$.[53]

Ion migration activation energy measurement

The ion migration activation energy is determined by measuring the temperature dependent electric conductivity in a structure of Au/perovskite /Au under 0.35 V μm^{-1} electrical field. The activation energy E_a can be extracted by fitting the raw data points with the Arrhenius equation,[31]

$$\sigma(T) = \mathrm{A}\exp\left(\frac{-E_a}{k_B T}\right) \tag{4}$$

where $\sigma(T)$ is the conductivity as a function of temperature T, A is a constant, and k_B is Boltzmann's constant. The activation energy can be derived from the slope of the $\ln(\sigma)$ -$1/(k_B T)$ relation. Although the conductivity (σ) of the $MA_{1-x}FA_xPbI_3$ film may arise from both electron/holes and mobile ions, the activation energy for electron/holes (E_a^{car}) and ion migration (E_a^{ion}) can be differentiated by measuring σ under both dark and light conditions,[31] since the photogenerated electron/holes should be the dominant contribution to conductivity under light.

Conductive-AFM (c-AFM)

A commercial AFM system (Cypher ES Environmental AFM, Asylum Research, USA) with sharp conductive single crystal diamond probes (AD-2.8-AS) were used to perform the c-

AFM measurements. The local dark-currents were taken in a N_2 atmosphere to avoid damage to the perovskite films during c-AFM measurements.

X-ray diffraction

X-ray diffraction measurements were undertaken for $MA_{1-x}FA_xPbI_3$ perovskite films on TiO_2-coated FTO-glass substrates by using a D2 PHASER (Bruker Corp.).

References

1 Ball, J. M. & Petrozza, A. Defects in perovskite-halides and their effects in solar cells. *Nat. Energy* **1**, 16149, doi:10.1038/nenergy.2016.149 (2016).

2 Yang, W. S. *et al.* Iodide management in formamidinium-lead-halide–based perovskite layers for efficient solar cells. *Science* **356**, 1376-1379, doi:10.1126/science.aan2301 (2017).

3 Luo, W. *et al.* Potential-induced degradation in photovoltaic modules: a critical review. *Energy Environ. Sci.* **10**, 43-68, doi:10.1039/C6EE02271E (2017).

4 Yoo, S.-H. *et al.* Identification of critical stacking faults in thin-film CdTe solar cells. *Appl. Phys. Lett.* **105**, 062104, doi:10.1063/1.4892844 (2014).

5 Fan, Z. *et al.* Ferroelectricity of $CH_3NH_3PbI_3$ perovskite. *J. Phys. Chem. Lett.* **6**, 1155-1161, doi:10.1021/acs.jpclett.5b00389 (2015).

6 Klein-Kedem, N., Cahen, D. & Hodes, G. Effects of Light and Electron Beam Irradiation on Halide Perovskites and Their Solar Cells. *Acc. Chem. Res.* **49**, 347–354, doi:10.1021/acs.accounts.5b00469 (2016).

7 Rothmann, M. U. *et al.* Structural and chemical changes to $CH_3NH_3PbI_3$ induced by electron and gallium ion beams. *Adv. Mater.* **30**, 1800629, doi:10.1002/adma.201800629 (2018).

8 Wehrenfennig, C., Eperon, G. E., Johnston, M. B., Snaith, H. J. & Herz, L. M. High Charge Carrier Mobilities and Lifetimes in Organolead Trihalide Perovskites. *Adv. Mater.* **26**, 1584-1589, doi:10.1002/adma.201305172 (2014).

9 Yin, W.-J., Shi, T. & Yan, Y. Unique Properties of Halide Perovskites as Possible Origins of the Superior Solar Cell Performance. *Adv. Mater.* **26**, 4653-4658, doi:10.1002/adma.201306281 (2014).

10 Stranks, S. D. Nonradiative Losses in Metal Halide Perovskites. *ACS Energy Lett.* **2**, 1515-1525, doi:10.1021/acsenergylett.7b00239 (2017).

11 Chen, B., Rudd, P. N., Yang, S., Yuan, Y. & Huang, J. Imperfections and their passivation in halide perovskite solar cells. *Chem. Soc. Rev.* **48**, 3842-3867, doi:10.1039/C8CS00853A (2019).

12 McKenna, K. P. Electronic Properties of {111} Twin Boundaries in a Mixed-Ion Lead Halide Perovskite Solar Absorber. *ACS Energy Lett.* **3**, 2663-2668, doi:10.1021/acsenergylett.8b01700 (2018).

13 Tan, C. S. *et al.* Heterogeneous Supersaturation in Mixed Perovskites. *Adv. Sci.* **7**, 1903166, doi:10.1002/advs.201903166 (2020).

14 Röhm, H., Leonhard, T., Hoffmann, M. J. & Colsmann, A. Ferroelectric Poling of Methylammonium Lead Iodide Thin Films. *Adv. Funct. Mater.* **30**, 1908657, doi:10.1002/adfm.201908657 (2020).

15 Rothmann, M. U. *et al.* Direct observation of intrinsic twin domains in tetragonal $CH_3NH_3PbI_3$ *Nat. Commun.* **8**, 14547, doi:10.1038/ncomms14547 (2017).

16 Weber, O. J., Charles, B. & Weller, M. T. Phase behaviour and composition in the formamidinium-methylammonium hybrid lead iodide perovskite solid solution. *J. Mater. Chem. A* **4**, 15375-15382, doi:10.1039/C6TA06607K (2016).

17 Weller, M. T., Weber, O. J., Frost, J. M. & Walsh, A. Cubic Perovskite Structure of Black Formamidinium Lead Iodide, α-$HC(NH_2)_2PbI_3$, at 298 K. *J. Phys. Chem. Lett.* **6**, 3209-3212, doi:10.1021/acs.jpclett.5b01432 (2015).

18 Charles, B., Dillon, J., Weber, O. J., Islam, M. S. & Weller, M. T. Understanding the stability of mixed A-cation lead iodide perovskites. *J. Mater. Chem. A* **5**, 22495-22499, doi:10.1039/C7TA08617B (2017).

19 Binek, A., Hanusch, F. C., Docampo, P. & Bein, T. Stabilization of the Trigonal High-Temperature Phase of Formamidinium Lead Iodide. *J. Phys. Chem. Lett.* **6**, 1249-1253, doi:10.1021/acs.jpclett.5b00380 (2015).

20 Pisanu, A. *et al.* The $FA_{1-x}MA_xPbI_3$ System: Correlations among Stoichiometry Control, Crystal Structure, Optical Properties, and Phase Stability. *J. Phys. Chem. C* **121**, 8746-8751, doi:10.1021/acs.jpcc.7b01250 (2017).

21 Rothmann, M. U. *et al.* Atomic-scale microstructure of metal halide perovskite. *Science* **370**, eabb5940, doi:10.1126/science.abb5940 (2020).

22 Lu, H. *et al.* Vapor-assisted deposition of highly efficient, stable black-phase FAPbI₃ perovskite solar cells. *Science* **370**, eabb8985, doi:10.1126/science.abb8985 (2020).

23 Pellet, N. *et al.* Mixed-Organic-Cation Perovskite Photovoltaics for Enhanced Solar-Light Harvesting. *Angew. Chem. Int. Ed.* **53**, 3151-3157, doi:10.1002/anie.201309361 (2014).

24 Dai, J. *et al.* Carrier Decay Properties of Mixed Cation Formamidinium–Methylammonium Lead Iodide Perovskite $[HC(NH_2)_2]_{1-x}[CH_3NH_3]_xPbI_3$ Nanorods. *J. Phys. Chem. Lett.* **7**, 5036-5043, doi:10.1021/acs.jpclett.6b01958 (2016).

25 Li, W.-G., Rao, H.-S., Chen, B.-X., Wang, X.-D. & Kuang, D.-B. A formamidinium-methylammonium lead iodide perovskite single crystal exhibiting exceptional optoelectronic properties and long-term stability. *J. Mater. Chem. A* **5**, 19431-19438, doi:10.1039/C7TA04608A (2017).

26 Green, M. A., Ho-Baillie, A. & Snaith, H. J. The emergence of perovskite solar cells. *Nat. Photonics* **8**, 506-514, doi:10.1038/nphoton.2014.134 (2014).

27 Tress, W. *et al.* Interpretation and evolution of open-circuit voltage, recombination, ideality factor and subgap defect states during reversible light-soaking and irreversible degradation of perovskite solar cells. *Energy Environ. Sci.* **11**, 151-165, doi:10.1039/C7EE02415K (2018).

28 Zhang, Y., Grancini, G., Feng, Y., Asiri, A. M. & Nazeeruddin, M. K. Optimization of Stable Quasi-Cubic $FA_xMA_{1-x}NH_3PbI_3$ Perovskite Structure for Solar Cells with Efficiency beyond 20%. *ACS Energy Lett.*, 802-806, doi:10.1021/acsenergylett.7b00112 (2017).

29 Snaith, H. J. *et al.* Anomalous Hysteresis in Perovskite Solar Cells. *J. Phys. Chem. Lett.* **5**, 1511-1515, doi:10.1021/jz500113x (2014).

30 Li, W. *et al.* Phase Segregation Enhanced Ion Movement in Efficient Inorganic $CsPbIBr_2$ Solar Cells. *Adv. Energy Mater.* **7**, 1700946, doi:10.1002/aenm.201700946 (2017).

31 Yuan, Y. *et al.* Photovoltaic Switching Mechanism in Lateral Structure Hybrid Perovskite Solar Cells. *Adv. Energy Mater.* **5**, 1500615-n/a, doi:10.1002/aenm.201500615 (2015).

32 Tan, S. *et al.* Steric Impediment of Ion Migration Contributes to Improved Operational Stability of Perovskite Solar Cells. *Adv. Mater.* **n/a**, 1906995, doi:10.1002/adma.201906995 (2020).

33 Haruyama, J., Sodeyama, K., Han, L. & Tateyama, Y. First-Principles Study of Ion Diffusion in Perovskite Solar Cell Sensitizers. *J. Am. Chem. Soc.* **137**, 10048-10051, doi:10.1021/jacs.5b03615 (2015).

34 Søndenå, R., Stølen, S., Ravindran, P., Grande, T. & Allan, N. L. Corner- versus face-sharing octahedra in $AMnO_3$ perovskites (A=Ca, Sr, and Ba). *Phys. Rev. B* **75**, 184105, doi:10.1103/PhysRevB.75.184105 (2007).

35 Zheng, X. *et al.* Improved Phase Stability of Formamidinium Lead Triiodide Perovskite by Strain Relaxation. *ACS Energy Lett.* **1**, 1014-1020, doi:10.1021/acsenergylett.6b00457 (2016).

36 C. Sinclair, D., M. S. Skakle, J., D. Morrison, F., I. Smith, R. & P. Beales, T. Structure and electrical properties of oxygen-deficient hexagonal $BaTiO_3$. *J. Mater. Chem.* **9**, 1327-1331, doi:10.1039/A900957D (1999).

37 Grey, I. E., Li, C., Cranswick, L. M. D., Roth, R. S. & Vanderah, T. A. Structure Analysis of the 6H–Ba(Ti, Fe^{3+}, Fe^{4+})$O_{3-\delta}$ Solid Solution. *J. Solid State Chem.* **135**, 312-321, doi:10.1006/jssc.1997.7652 (1998).

38 Lin, M.-H. & Lu, H.-Y. Hexagonal-phase retention in pressureless-sintered barium titanate. *Philos. Mag. A* **81**, 181-196, doi:10.1080/01418610108216627 (2001).

39 Rečnik, A. & Kolar, D. Exaggerated Growth of Hexagonal Barium Titanate under Reducing Sintering Conditions. *J. Am. Ceram. Soc.* **79**, 1015-1018, doi:10.1111/j.1151-2916.1996.tb08541.x (1996).

40 Rečnik, A., Bruley, J., Mader, W., Kolar, D. & Rühle, M. Structural and spectroscopic investigation of (111) twins in barium titanate. *Philos. Mag. B* **70**, 1021-1034, doi:10.1080/01418639408240270 (1994).

41 Jia, C. L., Urban, K., Mertin, M., Hoffmann, S. & Waser, R. The structure and formation of nanotwins in $BaTiO_3$ thin films. *Philos. Mag. A* **77**, 923-939, doi:10.1080/01418619808221220 (1998).

42 Hagemann, H.-J. & Ihrig, H. Valence change and phase stability of 3d-doped $BaTiO_3$ annealed in oxygen and hydrogen. *Phys. Rev. B* **20**, 3871-3878, doi:10.1103/PhysRevB.20.3871 (1979).

43 Shibahara, H. Electron microscope study of the structure of SrMnO3−x with planar defect. *J. Mater. Res.* **6**, 565-573, doi:10.1557/JMR.1991.0565 (1991).

44 Adkin, J. J. & Hayward, M. A. BaMnO3-x Revisited: A Structural and Magnetic Study. *Chem. Mater.* **19**, 755-762, doi:10.1021/cm062055r (2007).

45 Liu, N. & Yam, C. First-principles study of intrinsic defects in formamidinium lead triiodide perovskite solar cell absorbers. *Phys. Chem. Chem. Phys.* **20**, 6800-6804, doi:10.1039/C8CP00280K (2018).

46 Azpiroz, J. M., Mosconi, E., Bisquert, J. & De Angelis, F. Defect migration in methylammonium lead iodide and its role in perovskite solar cell operation. *Energy Environ. Sci.* **8**, 2118-2127, doi:10.1039/C5EE01265A (2015).

47 Walsh, A. & Zunger, A. Instilling defect tolerance in new compounds. *Nat. Mater.* **16**, 964, doi:10.1038/nmat4973 (2017).

48 Zhu, Y. *et al.* Effects of strain on defect structure in II-VI green color converters. *J. Appl. Phys.* **108**, 123104, doi:10.1063/1.3517069 (2010).

49 Chen, T. *et al.* Origin of long lifetime of band-edge charge carriers in organic–inorganic lead iodide perovskites. *Proc. Natl. Acad. Sci.* **114**, 7519-7524, doi:10.1073/pnas.1704421114 (2017).

50 Yang, J. *et al.* Acoustic-optical phonon up-conversion and hot-phonon bottleneck in lead-halide perovskites. *Nat. Commun.* **8**, 14120, doi:10.1038/ncomms14120 (2017).

51 Kim, J. *et al.* Nucleation and Growth Control of $HC(NH_2)_2PbI_3$ for Planar Perovskite Solar Cell. *J. Phys. Chem. C* **120**, 11262-11267, doi:10.1021/acs.jpcc.6b02443 (2016).

52 Huang, F. *et al.* Gas-assisted preparation of lead iodide perovskite films consisting of a monolayer of single crystalline grains for high efficiency planar solar cells. *Nano Energy* **10**, 10-18, doi:10.1016/j.nanoen.2014.08.015 (2014).

53 Chen, W. *et al.* Nanoscale Characterization of Carrier Dynamic and Surface Passivation in InGaN/GaN Multiple Quantum Wells on GaN Nanorods. *ACS Appl. Mater. Interfaces* **8**, 31887-31893, doi:10.1021/acsami.6b11675 (2016).

Acknowledgements

The authors thank the reviewers for their expert criticisms that significantly improved this manuscript. This work has been financially supported by National Natural Science Foundation of China (NSFC 91963209) and the Australian Government through the Australian Renewable Energy Agency and the ARC Discovery Grant DP150104483. W.L., M.R., U.B and Y.B.C. acknowledges the support from the Australian Centre for Advanced Photovoltaics. The authors acknowledge use of facilities within the Monash Centre for Electron Microscopy, a node of Microscopy Australia, and the Monash X-Ray Platform. M.R. and W.L. are grateful to A/Prof Laure Bourgeois for expert advice on the operation of the JEOL 2100F. W.L. acknowledges the support from National Natural Science Foundation of China (NSFC 51802241) and the Fundamental Research Funds for the Central Universities (WUT: 2019IVB055 and 2019IVA066). Y.Z. is supported by the Hong Kong Research Grants Council (Project No. 15305020) and the Hong Kong Polytechnic University grant (Project No. ZVRP).

Author contributions

W.L., M.R. and Y.Z contributed equally to this work. W.L., M.R., U.B., Y.B.C. and J.E conceived and designed the experiment. W.L. and M.R. carried out sample preparation. W.L. and M.R. did electron microscopy and W.L., M.R., Y.Z and J.E analysed the data. W.L., Y.Y., and C.Y. did temperature dependent conductivity tests and data analysis. W.L. is grateful to Dr. Ren Zhu from Oxford instruments for operation of c-AFM. W.L., M.R., Y.Z and J.E wrote the manuscript. All authors contributed to the discussion of the results and revision of the manuscript.

Corresponding authors

Correspondence to Joanne Etheridge, Yi-Bing Cheng or Udo Bach.

Competing interests

The authors declare no competing interests.

Additional information

Supplementary Information:

Figures 1-26

Tables 1-4

Data availability

All data generated or analysed or during this study are included in the published article and its Supplement Information and Source Data files. Source data are provided with this paper.

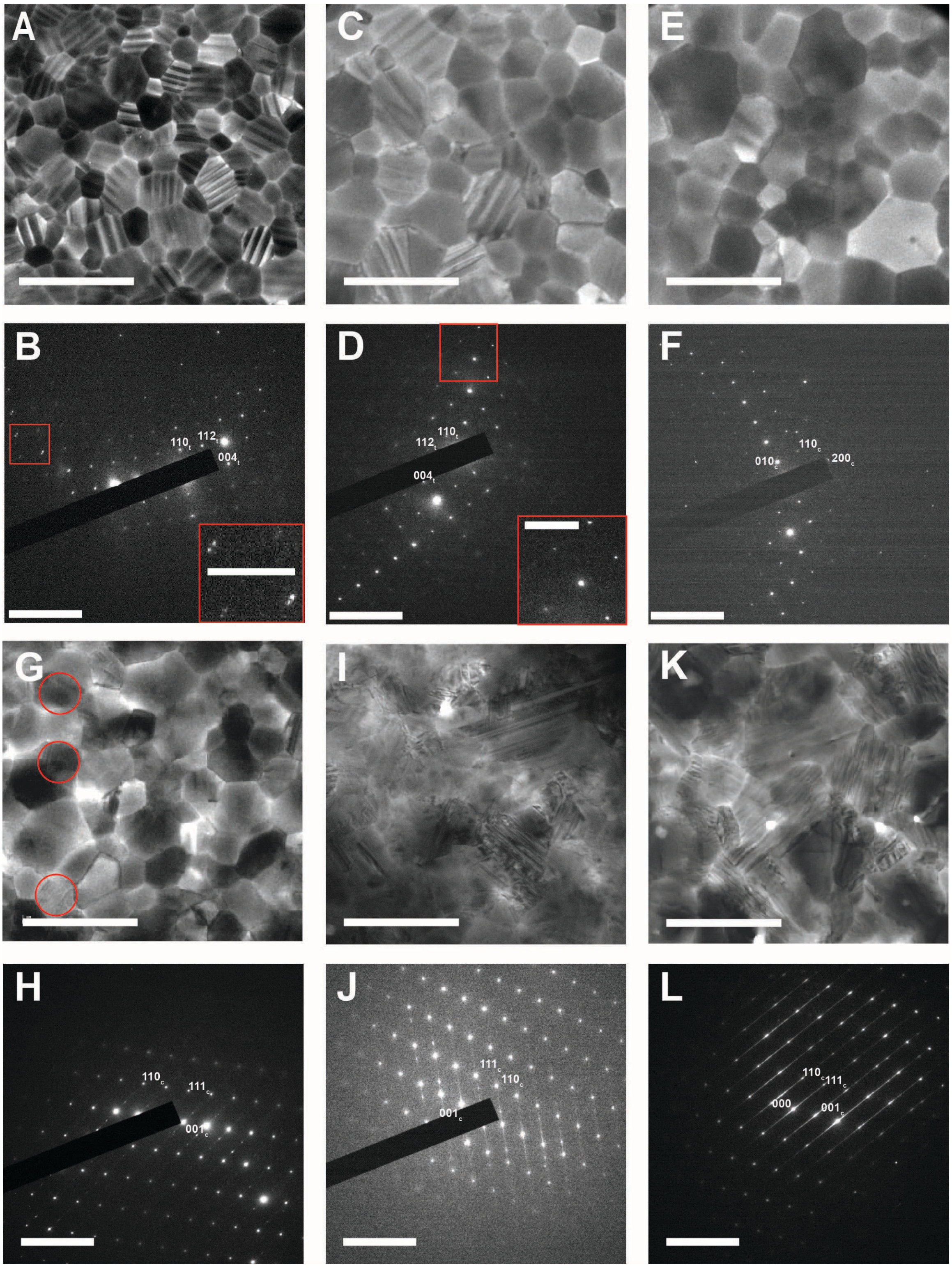

Figure 1. Microstructural characteristics. (a,c,e,g,i,k) Bright field TEM images and (b,d,f,h,j,l) SAED patterns taken from $MA_{1-x}FA_xPbI_3$ thin films, with (a-b) x=0, (c-d) x=0.1, (e-f) x=0.2, (g-h) x=0.5, (i-j) x=0.85 and (k-l) x=1. Scale bars are: (a,c,e,g,i,k) 1 µm, (b,d,f,h,j,l) 5 nm^{-1}, and (b,d) insert 2 nm^{-1}.

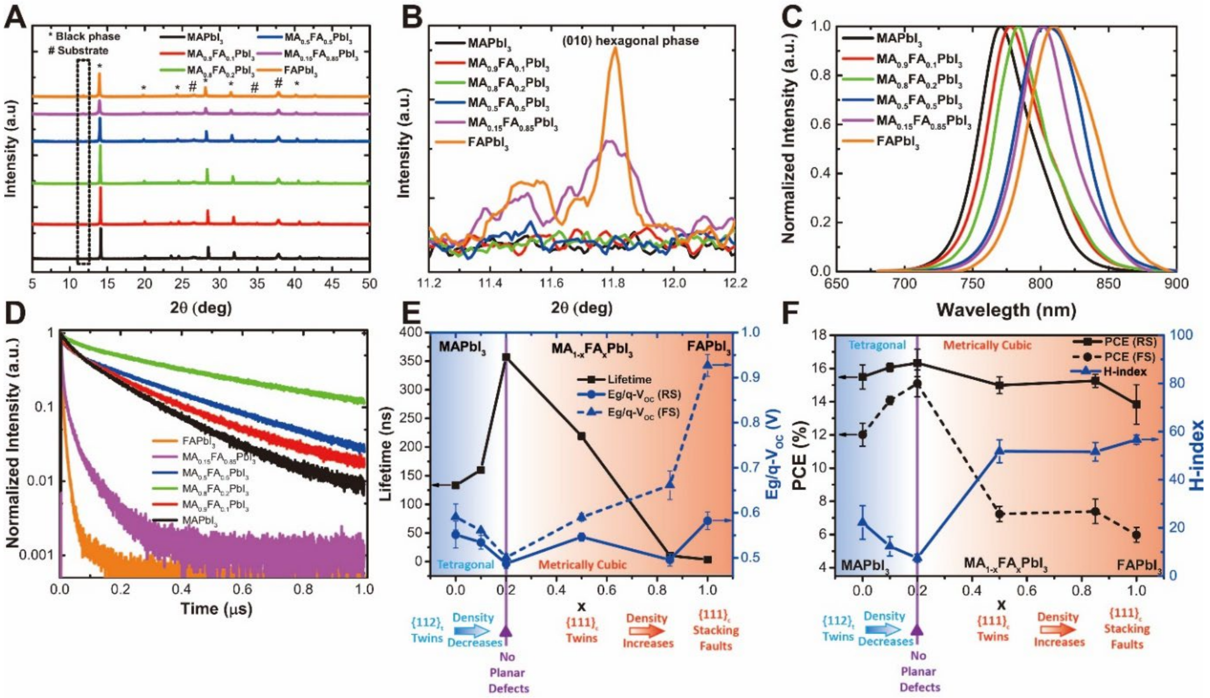

Figure 2. Material characterisations and device properties. (a) Powder X-ray diffraction patterns of the mixed cation $MA_{1-x}FA_xPbI_3$ thin films, (b) Enlarged view of the peaks in the dotted box in (a) showing elimination of hexagonal phase with decreasing x, (c) PL spectra of the $MA_{1-x}FA_xPbI_3$ compounds studied showing a general trend of red-shift with increased FA-content, indicating a decrease of bandgap, (d) PL decay traces of the studied compounds. (e) Corresponding charge carrier lifetimes and calculated V_{OC} deficit ($E_g/q-V_{OC}$), (where q denotes the elementary charge) as a function of x in the $MA_{1-x}FA_xPbI_3$ compounds studied, (f) The average power conversion efficiencies calculated from the reverse and forward scans (RS and FS, respectively) and the corresponding hysteresis indices. The corresponding observations of intragrain planar defects are overlayed in (e) and (f). $MA_{0.8}FA_{0.2}PbI_3$ shows the longest carrier lifetime, lowest V_{OC} deficits, highest efficiencies in both scanning directions, as well as the lowest hysteresis. Statistics of solar cell performance are provided in the Supplementary Figure 16. The curved lines do not indicate measurements but serve to aid the eye showing a peak at $MA_{0.8}FA_{0.2}PbI_3$.

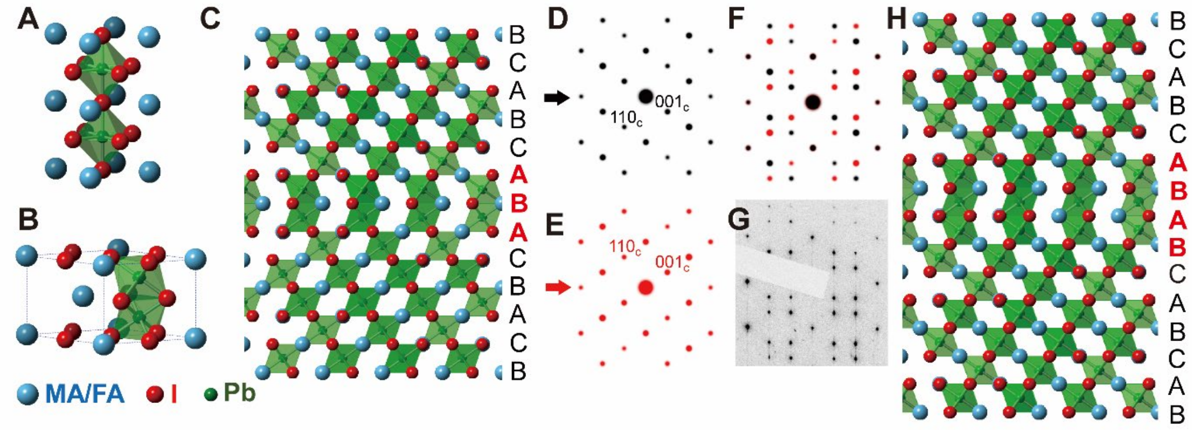

Figure 3. Schematic of proposed $\{111\}_c$ twinning structure in $MA_{1-x}FA_xPbI_3$. (a-c) Atomic model for (a) the cubic perovskite phase, (b) the 2H hexagonal phase, and (c) a $\{111\}_c$ twin structure inside the cubic perovskite matrix, with a twin boundary at the middle. (d-e) Calculated SAED patterns from (d) the upper and (e) lower domains, respectively. (f) Calculated SAED patterns from the overlap of (d) and (e) showing the $^1/_3 111_c$ reflection spots. (g) Experimental SAED pattern showing the $^1/_3 111_c$ reflection spots from a twin boundary. (h) Atomic model for a $\{111\}_c$ stacking fault inside the cubic perovskite matrix. The 2H hexagonal phase can be identified by the *ABAB* stacking sequence at both (c) the twin boundary and (h) the stacking fault. $\{111\}_c$ SFs can also be described as two consecutive monolayer twins. The 2H hexagonal phase generated by these planar defects is in effect a lamella of the photo-inactive, so-called "yellow phase" of δ-$FAPbI_3$. Note that here FA/MA cations are simplified as spheres without considering their molecular shapes.

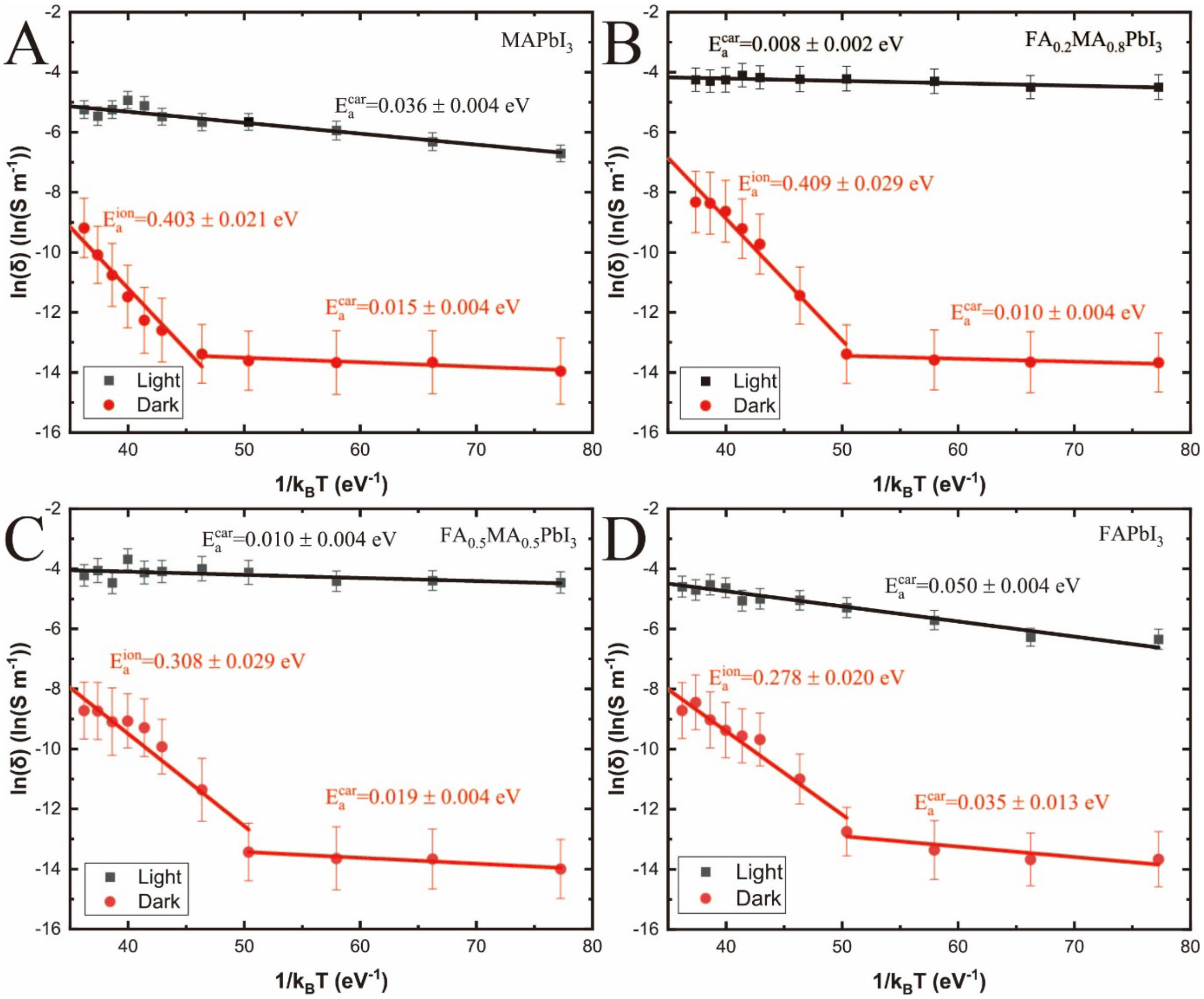

Figure 4: **Ion migration activation energy.** Arrhenius plot of the conductivity of the (a) MAPbI$_3$, (b) MA$_{0.8}$FA$_{0.2}$PbI$_3$, (c) MA$_{0.5}$FA$_{0.5}$PbI$_3$ (d) FAPbI$_3$ films under dark (Red) and illumination (black, the light intensity is 0.25 mW cm^{-2}).